



This is a repository copy of *Quantification of sub-surface railhead material damage due to composite endpost materials of insulated rail joints for cyclic wheel loadings*.

White Rose Research Online URL for this paper:
<https://eprints.whiterose.ac.uk/159973/>

Version: Accepted Version

Article:

Kumar Mandal, N., Lewis, R. orcid.org/0000-0002-4300-0540 and Wen, Z. (2020) Quantification of sub-surface railhead material damage due to composite endpost materials of insulated rail joints for cyclic wheel loadings. *Engineering Failure Analysis*, 113. 104562. ISSN 1350-6307

<https://doi.org/10.1016/j.engfailanal.2020.104562>

Article available under the terms of the CC-BY-NC-ND licence (<https://creativecommons.org/licenses/by-nc-nd/4.0/>).

Reuse

This article is distributed under the terms of the Creative Commons Attribution-NonCommercial-NoDerivs (CC BY-NC-ND) licence. This licence only allows you to download this work and share it with others as long as you credit the authors, but you can't change the article in any way or use it commercially. More information and the full terms of the licence here: <https://creativecommons.org/licenses/>

Takedown

If you consider content in White Rose Research Online to be in breach of UK law, please notify us by emailing eprints@whiterose.ac.uk including the URL of the record and the reason for the withdrawal request.



eprints@whiterose.ac.uk
<https://eprints.whiterose.ac.uk/>

Quantification of sub-surface railhead material damage due to composite endpost materials of insulated rail joints for cyclic wheel loadings

Nirmal Kumar Mandal¹, Roger Lewis² and Zefeng Wen³

¹Central Queensland University, Centre for Railway Engineering, Queensland 4702, Australia

²The University of Sheffield, Department of Mechanical Engineering, Sheffield, S1 3JD, UK.

³Southwest Jiaotong University, Chengdu, Sichuan 610031, P.R. China

ABSTRACT

This study focusses on a 3D finite element analysis to investigate damage of sub-surface railhead material at insulated rail joints (IRJs) considering different composite endpost materials (fibreglass, nylon 66 and polytetrafluoroethylene). At the wheel/rail contact patch on IRJs, vertical wheel impacts up to a total of 2000 cycles are applied. Damage parameters exhibit a *vertical flat type* damage pattern for a depth up to 8mm initially and, as the cyclic loading increases, the flat damage pattern changes to a *horizontal bell-shape* pattern. The results indicate that fibreglass is a better endpost material to control sub-surface railhead material damage.

Keywords: Rail joints; Composite material endpost; FEA; Sub-surface damage; Cyclic ratchetting; Elastoplastic material behaviour.

1.0 INTRODUCTION

Conventional mechanical bolted joints are used for connecting strings of continuous welded rail (CWR), for temporary repairs, and in sharp curves where rapid wear forces regular rail replacements. However, IRJs are very important in controlling trains on a railway track using electrical signalling blocks (Figure 1) and can also be used in locating broken rails. The bending rigidity of an IRJ is only two-thirds that of continuous rail. Consequently, larger stresses and deflections are experienced in the vicinity of IRJs. It is, therefore, necessary to give proper attention in designing the geometrical configuration of IRJs, focussing on composite endpost materials and other parameters to reduce plastic flow and stress states of the rail material.

There is a tendency of reducing the number of IRJs in CWR track, but it is deemed impossible to replace them fully. Therefore, proper attention should be given to the design of the

components of IRJs including endpost materials as they are one of the weakest links of the track structure.

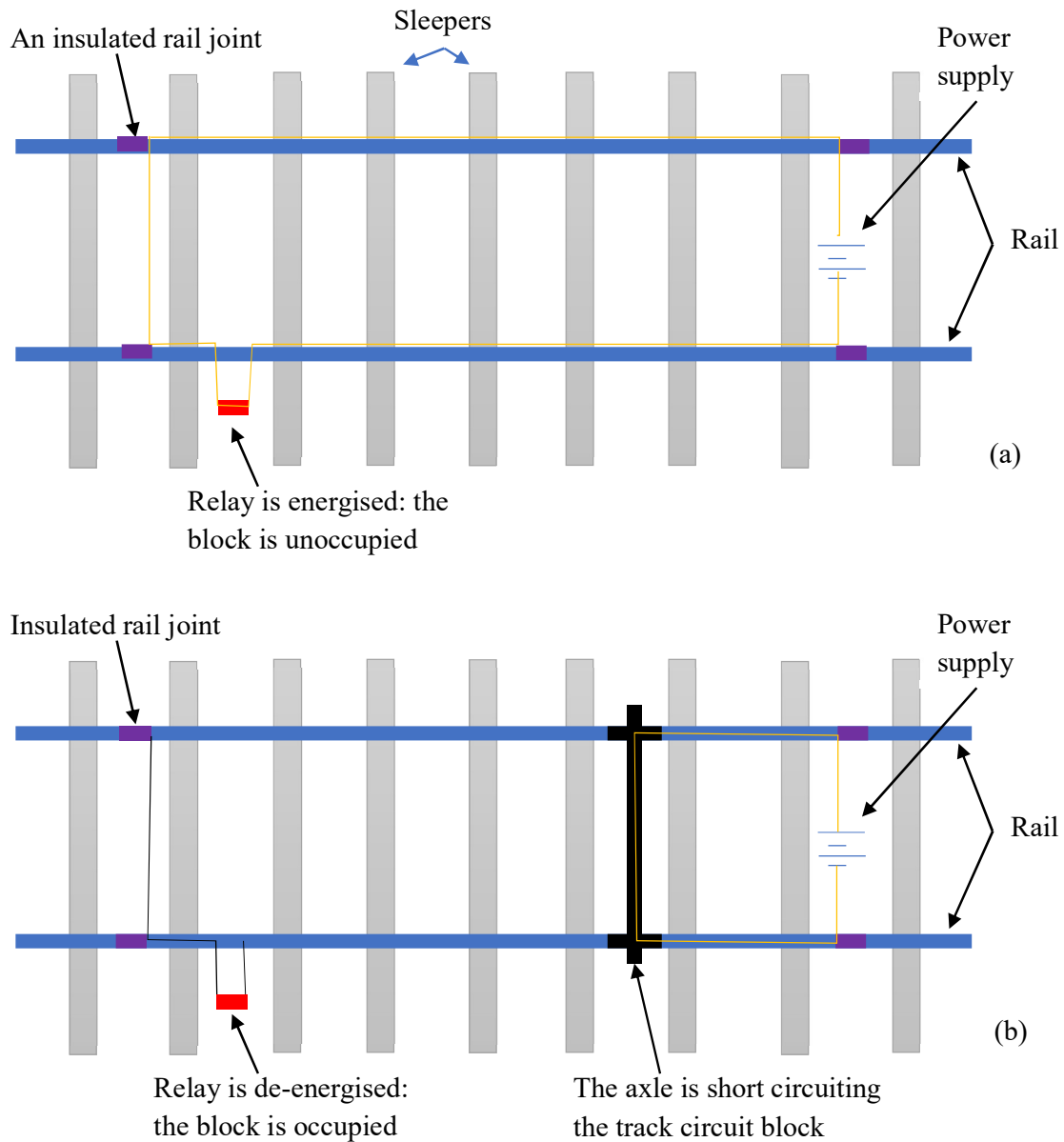


Figure 1: Railway electrical track circuit: signalling block - (a) unoccupied, (b) occupied

Polymers, composite materials, thermosetting plastics and thermoplastics have wide industrial applications. The popular polymers and composite materials are: fibreglass (fb), nylon (ny), polytetrafluoroethylene (ptfe), polycarbonate (pc), polystyrene (ps), polypropylene (pp), aramid (kevlar 49), carbon fibre-epoxy, polyvinylchloride (pvc), melamine formaldehyde, urea formaldehyde etc. Composite and polymer materials are also useful in railway track. In IRJs,

fb is the most commonly used endpost material in Australian railways. Nylon is primarily used in the UK. Another popular endpost material is ptfе.

There are a few early papers available presenting performance focussing on mechanical rail joints [1, 2] and more recently such papers are also focusing on IRJs through experiments and numerical modelling [3, 4, 5, 6]. However, the effects of endpost materials on mechanical behaviour and railhead and sub-surface material damage due to cyclic wheel loading has not yet been examined in full. There is some literature which is generally focussed on residual stresses and strain and plastic deformation information relating to the top surface of the railhead at IRJs. Recently, Mandal [7, 8] studied the effects of three endpost materials (fb, ny and ptfе) on railhead damage relating to plastic deformation of railhead top material in the vicinity of the IRJs. Some studies also focussed on impact factor due short-pitch wavelength defects [9] and railhead material degradation [10 - 15]. Beaty et al. [12] showed by experiments using twin-disc testing that metal flow of rail steel over the endpost, called lipping, was insensitive to the thickness of endposts. In addition, higher strength rail steel and endpost material could reduce the lipping rate of railhead steel material. Mandal [16] carried out FEA simulation studies considering 5mm and 10mm endpost thicknesses and pointed out that longitudinal plastic flow (metal flow) for 10mm endpost thickness of IRJ was greater than that of 5mm endpost rail joint for 100 loading cycles, suggesting a thicker endpost joint was more prone to progress top railhead damage, but at the sub-surface depth, the effect of endpost thickness was insignificant.

A detailed rail sub-surface damage pattern analysis is deemed important for product design and development purposes. Research studies should address a few key points of mechanical behaviour of IRJs due to the soft endpost materials used. They are:

- Wheel load sharing by endpost material is significantly lower compared to rail and the degree of the load sharing is based on the Young's Modulus values of endpost materials. Thereby different stress levels can result in the railhead material. Therefore, there can potentially be a hypothesis linking endpost material properties and the degree of railhead damage.
- Railhead damage through plastic flow of rail steel over the top of the endpost material is not sensitive to thickness of endposts, but rather to strength of railhead steel and endpost materials. Can it be assumed that there is a similar trend for the effect of endpost

thickness over the extent of vertical dynamic wheel loads and subsequent top surface and sub-surface damage of railhead material?

- Ranking of endpost material influence on railhead stress levels at different loading cycles is necessary.
- Detailed information on the location of sub-surface plastic zones of railhead material is necessary. Is this information dependent on loading cycles?
- Which stress component is responsible for damaging the top railhead and sub-surface material?

In order to understand more about the points above, it is necessary to carry out a detailed study of sub-surface damage of railhead material for IRJs using some popular endpost materials (fb, ny and ptfe), benchmarking the mechanical behaviour of ny and ptfe against the most commonly used fb. This work advances a previous published study [17].

2.0 METHODS

A 3D finite element analysis (FEA) is conducted to model IRJs through the application of a global model and a sub-model for local damage analysis as described in Mandal and Dhanasekar [18]. A cyclic vertical wheel load is applied on the railhead top surface in the vicinity of an IRJ in a pressure form considering a non-Hertzian pressure distribution. Section 2.1 discusses a global FEA rail joint model of a conventional Australian 5mm endpost thickness IRJ, and Section 2.2 discusses a sub-model of part of the railhead in the vicinity of the IRJ. A non-linear isotropic/kinematic hardening material behaviour was considered for the contact zone of the wheel/rail interface for 60kg/m head-hardened rail. A detailed description of sub-modelling of the IRJ and of elasto-plastic material behaviour was presented in [18].

2.1 A rail joint global model

There are two types of insulated rail joints: square joints cut at 90° to the rail longitudinal axis (present study) and angle (mitred) joints cut at 15° to the axis. The geometric design of both types of rail joints can be carried out in the part module of Abaqus employing 90° cut or 15° cut with longitudinal axis. Figure 2(a) shows a part of the FEA model of the IRJ. Total length of the IRJ model considered for this study is 12m. This length is deemed enough when considering boundary conditions of a finite rail piece [19]. A 2.4m length is a solid rail model taken from the 12m rail with a 1/20 rail cant position as per Australian Standard 1085.12 [20]. Two beam models (not shown), each 4.8m long, are connected to the ends of the solid rail model by

equation constraints in ABAQUS to ensure zero displacement and rotation of beams and rail relative to one another. This ensures all six DOFs are transferred from the solid rail model to the beam models. Other parameters are: 5mm endpost thickness, 6 bolt joint plates, IRJ is centrally suspended between two adjacent sleepers (Figure 2(a)), 0.7m centre to centre sleeper spacing. The geometric design of an IRJ follows the requirements of the Australian Standard AS 1085:12 [20] using a 60kg rail. This is a simplified IRJ model drawn in a single piece with rail, joint bar, nut, bolt, insulation material and endpost, not drawn separately and then assembled using constraints. The partition options in ABAQUS are used to model each part, employing their appropriate material properties [20]. A 3mm round slot around the bolt of 27mm diameter is introduced to create a gap of 3mm between rail web and the bolt shank. Similar to the endpost tie connection to the rail ends, the insulation materials between rail web and joint bar are rigidly connected using a tie constraint.

For operational parameters, conditions of the local heavy haul coal routes such as 26.6 tonnes axle load, 80km/hr train speed etc. are considered. For calculating wheel load on IRJs, the axle load is rounded to 30 tonnes and corresponding static wheel load is 150kN. As the wheels move over the IRJs, the dynamic impact factor of 1.16 [21] is used for 80km/hr train speed to calculate a vertical dynamic wheel load on IRJs of 174kN from a static wheel load of 150kN. As the modelling considers only vertical impact of wheel loads on IRJs, wheel/rail longitudinal force at the contact patch is not considered. Figure 2(b) shows the 174kN wheel loading in pressure form on the IRJ with 2500MPa as a peak pressure. The wheel/rail contact pressure was idealised as a stepwise function (Figure 3) and applied normal to the railhead top surface in a way that the maximum peak pressure of 2500MPa occurred at the rail end because of pressure singularity at the rail end. The pressure distribution covers the contact patch on both rails ends and endpost, suggesting the wheel loads are approaching to the rail joint. Total wheel load of 174kN can be calculated by multiplying respective pressure values to their contact areas. As the wheel impact is changing cyclically from 0kN to 174kN, consequently the magnitude of pressure peaks is also changing from 0MPa to its maximum peak values such as 2500MPa for example. It was managed by the 'amplitude' function of ABAQUS by putting '0' for no loading and '1' for full loading within a time interval. Figure 3 shows a longitudinal (full contact patch, '2a') and lateral (half contact patch, 'b') pressure distributions.

Bolt loads of 200kN [10] in each bolt are applied on bolt cross-sections. ABAQUS's part and section modules are used to construct the IRJ model and apply homogeneous section and elastic-plastic material properties respectively. The top critical area of the head of the rail (dark

part of Figure 2(a)) is defined with high mesh density to account for elastic-plastic material deformation. The high mesh density part is shown separately in Figure 2(b) and is connected to the remaining part of the IRJ model by tie constraints. The other part of the IRJ model is elastic.

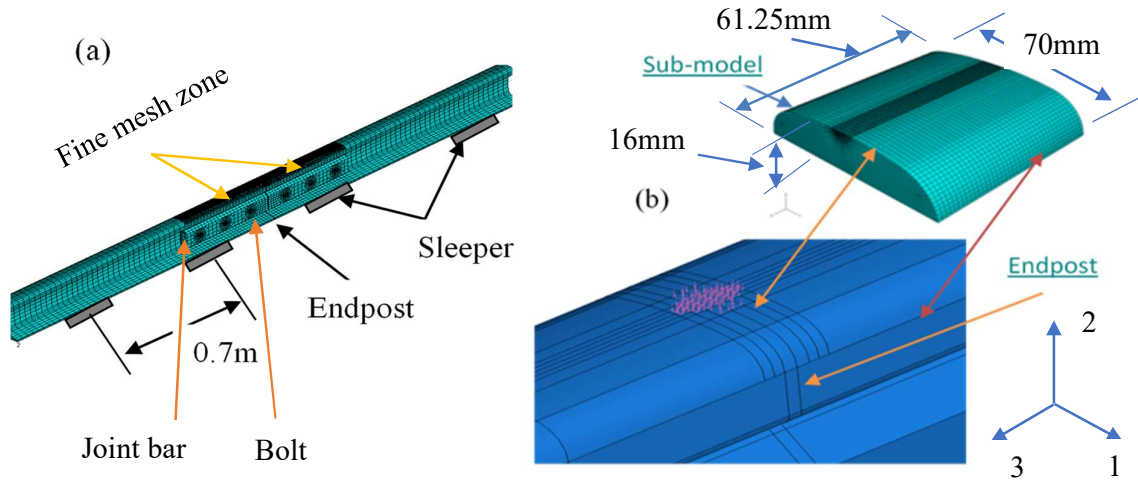


Figure 2: (a) FEA global model of IRJ and (b) FEA sub-model showing loading on IRJ and location of sub-model

Figure 2 (b) indicates the coordinate system directions where 3 indicates the longitudinal direction, 2 the vertical direction and 1 the lateral direction and the figure includes the dimensions of the sub-model.

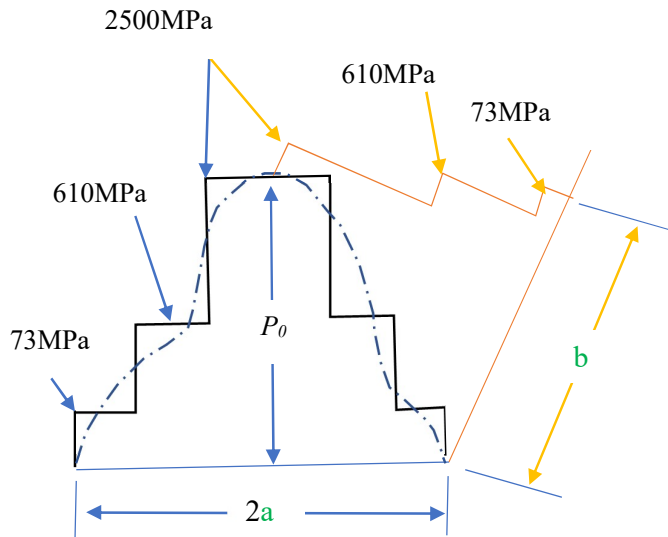


Figure 3: A non-Hertzian wheel impact loading model on the contact patch showing a stepwise pressure distribution both in longitudinal and lateral directions.

Table 1 presents the Young's Modulus and Poisson's ratio of rail steel and endpost materials, and Table 2 contains the elastic-plastic material properties of the top surface of the head-hardened rail.

Table 1: Elastic rail steel and endpost material properties [22]

Name	Young's Modulus (MPa)	Poisson's Ratio
Head hardened rail steel	207000	0.3
Fibreglass (fb)	45000	0.19
Nylon 66 (ny)	1590	0.39
PTFE (ptfe)	400	0.46

Table 2: Elastic-plastic properties of rail top surface material (the high mesh density part shown in Figure 2(a)) [22]

σ_y (MPa)	K_∞ (MPa)	b'	c (MPa)	γ
780	152	3.97	393000	8.3

Elastic properties include Young's Modulus and Poisson's Ratio of the solid rail material, joint bars, bolts and the various endpost materials (fb, ny and ptfe). The elastic-plastic material properties, on the other hand, include material and hardening parameters. The definitions of all parameters are: K_∞ is the maximum change in size of the yield surface, σ_y is the yield strength of rail steel, b' is the rate at which the size of the yield surface changes as plastic straining develops γ is the rate at which the kinematic hardening modulus decreases with the increase of plastic deformation, and c is the kinematic hardening modulus.

2.2 A rail joint sub-model

The sub-modelling is a local FEA modelling strategy for a more accurate simulation study. A critical section of the top surface of the railhead in the vicinity of the free rail ends of the IRJ

(Figure 2 (b)) is employed for a sub-modelling study, keeping the same magnitude of x, y, z coordinates. Figure 2 (b) also shows the location of the sub-model part in the global rail joint model. Four sub-model meshes were considered in this study for an initial mesh convergence study to select an optimum mesh (mesh 3). The numbers of nodes and elements of the different meshes are shown in Table 3.

Table 3: Node and element numbers of four sub-model meshes

Meshes	Nodes	Elements
Mesh 1	13,338	11,492
Mesh 2	29,376	26,180
Mesh 3	46,166	41,600
Mesh 4	90,240	83,444

2.3 Material modelling

Both elastic and elasto-plastic material modelling concepts are employed in this paper. In the contact zone at the rail top surface (fine mesh zone, Figure 2(a)), the contact stress level is higher than that of the yield point of the rail material. Therefore, a nonlinear isotropic/kinematic material hardening model approach, called combined material hardening model in ABAQUS, is used to mimic the material behaviour (Table 2) for cyclic loadings. For the other mesh zones of rail, an elastic rail material model is used (Table 1).

As in the contact zone where the rail top surface deforms elasto-plastically and incremental plasticity theory is employed in which mechanical strain rate is decomposed into two parts: an elastic part and a plastic part. The core of this theory is based on a yield surface, evolution laws and flow rule. The nonlinear isotropic/kinematic hardening material model is good for ratchetting and relaxation, Bauschinger effects and plastic shakedown. In this material model, isotropic and kinematic laws are coupled. As a result, the yield surface is free to change its shape and size and free to move in stress space. The isotropic law is also responsible for a decay in ratchetting rate. The yield stress in material models is generally defined by von-Mises yield surface, kinematic hardening rule and associated plastic flow rules.

The von-Mises yield surface is defined as:

$$\phi(\sigma, X, K) = \sqrt{\frac{3}{2}} |\tau_{dev}| - K - \sigma_y \quad (1)$$

$$\text{with } \tau_{dev} = \sigma_{dev} - X_{dev}, |\tau_{dev}| = \sqrt{\tau_{dev} : \tau_{dev}}$$

where $|\tau_{dev}|$ is the equivalent von-Mises stress, σ_{dev} is the deviatoric stress tensor (defined as $\sigma_{dev} = \sigma - pI$, where σ is the stress tensor, p is the equivalent pressure stress and I is the identity tensor), σ_y is the yield stress, K is the drag stress, X_{dev} is the deviatoric part of the back stress tensor and the operator ‘:’ defines the contraction $x:y = x_{ij}y_{ij}$.

The non-linear hardening model captures both isotropic and kinematic hardening. The isotropic hardening law can be presented as:

$$\dot{K} = \lambda b \left(1 - \frac{K}{K_\infty}\right) \quad (2)$$

This law indicates a decay in the ratchetting rate where K_∞ is the saturated drag stress due to isotropic hardening, λ is the plastic multiplier, and b governs the initial rate of isotropic hardening. Both b and K_∞ are material constants.

A non-linear kinematic hardening model relies on the steady accumulation of plastic strain. The law presents as:

$$\dot{X} = \lambda \left(c \sqrt{\frac{2}{3}} n_{dev} - \gamma X \right) \quad (3)$$

where $n_{dev} = \frac{\tau_{dev}}{|\tau_{dev}|}$ and c and γ are material parameters.

The Young’s Modulus of the composite endpost materials are much less (nearly 1/500th) than that of rail material, so a small portion of wheel load is shared by the endpost materials. Eventually, an elastic material behaviour is considered for endpost material in the simulation (Table 1).

Other steps such as assembly, step functions etc. are carried out accordingly. An eight node fully integrated trilinear brick element (C3D8) is used for all parts in the solid rail model through the mesh model employing the structural meshing technique. The job module is used to complete the simulation statically. Time dependent displace functions from odb files are further employed to carry out the local sub-modelling (Figure 2(b)) analysis.

3.0 RESULTS AND DISCUSSIONS

Output database (odb) files obtained from FEA global and sub-models are considered here to rank railhead sub-surface plastic deformation due to the three endpost materials used: fb, ny and ptf. A few damage parameters are considered to quantify the railhead sub-surface damage namely equivalent plastic strain (PEEQ), residual vertical plastic strain (PE22) and residual

von-Mises stresses (von) for 50, 1000 and 2000 vertical wheel load cycles. There are six strain and stress components in addition to the PEEQ and von-Mises stress components in the odb files. Of those, the PEEQ represents the average of all strain contributions and it accumulates over the loading cycles. The von-Mises stress component is also the average of stress components present. As the PEEQ and von-Mises components represent the average values of different strain and stress components respectively, this study populates mainly these datasets. The value of PE22 can be the main contributor of the PEEQ for this type of loading, hence the PE22 data are populated. The longitudinal shear strain PE23 can be a main contributor of railhead damage. However, for a vertical wheel impact loading without longitudinal traction forces at the contact patch, the strain component is not so significant [22]. Therefore, in this section, simulation results based on residual strains (PEEQ and PE22) are initially presented followed by residual von-Mises stress results.

Both plastic strain and equivalent plastic strain are a measure of sub-surface railhead material damage, quantifying plastic deformation forming a plastic zone. Plastic strain represents a strain variation after one loading cycle. However, PEEQ yields an accumulation of all plastic components throughout multiple cycles. The residual components of stress and strain are the values of those when there is no wheel load on the rail top material. The stress and strain values are locked into the material.

3.1 Strain results

Figure 4 shows a contour plot of PEEQ at the end of 2000 loading cycles. The influence of fb endpost material on rail end damage shows a clear indication that all the plastic strain components are accumulated at the shallow sub-surface zone, hence this zone can be regarded as a critical zone for crack initiation. Figure 5 also shows the accumulation pattern of all plastic strains at the top of the rail end for all three endpost materials. This shows an important extent of damage for a period of 3 second (1500 loading cycles) which illustrates a continuous progressive damage pattern of rail top material in every cycle which will continue until the ductility of the rail material is exhausted.

Figure 5 articulates that the fb endpost material performs better compared with the other two in considering continuous railhead damage. The ny endpost material is the worst for the same consideration. This is the opposite to what was noted in the literature recently [23] considering other aspects of the study. Among the three endpost materials considered, ny yields a transition of material behaviour from ratchetting to alternating plasticity at a lower number of loading

cycles compared to the other two. Through a twin disc experiment, Beaty et al. [12] showed that stiffer endpost material led to less deformation of the railhead material which is similar to these results. Although the PEEQ plots look to be linear, they bend marginally downwards over time showing a decay in ratchetting rate. A clear decay trend can be expected for a longer simulation time.

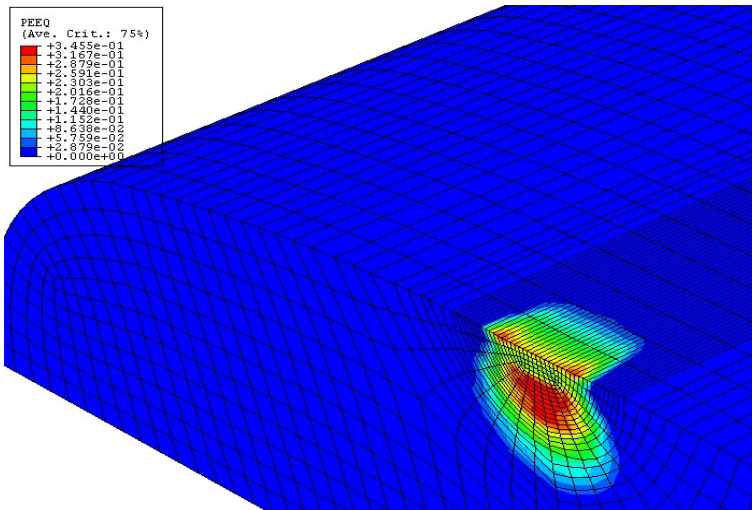


Figure 4: A contour plot of PEEQ for rail end material after 2000 loading cycles for fb endpost

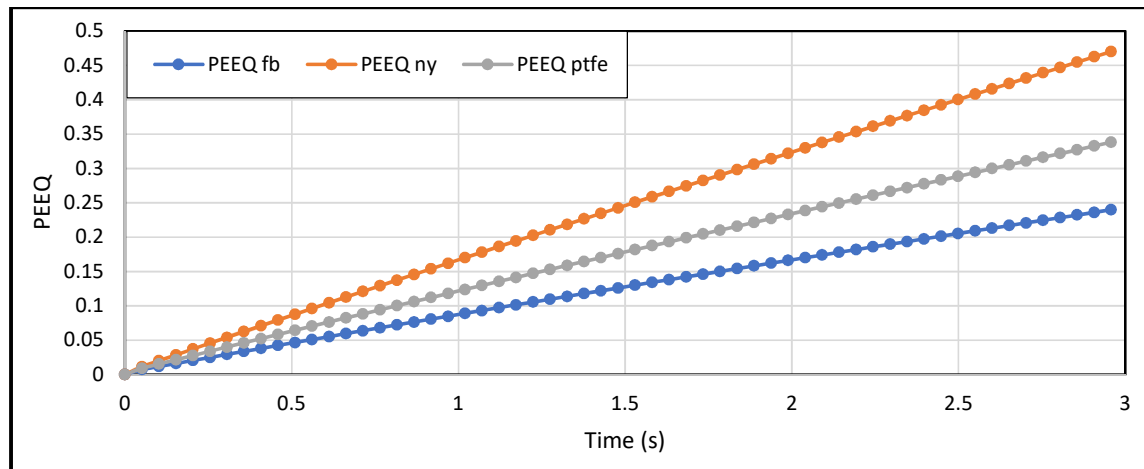


Figure 5: PEEQ of the rail top material at the rail end due to three endpost materials

Figures 6 to 8 show the variation of residual vertical plastic strain (PE22) in the railhead sub-surface for fb, ny and ptfe after 50, 1000 and 2000 loading cycles. It is evident in Figure 6 for 50 loading cycles that, for a shallow depth up to 1mm, the PE22 is increasing regularly for all endpost materials. However, from 1 mm to 7 mm, there is not much change in the residual vertical plastic strain, showing an almost constant value in the sub-surface zone for all endpost

materials. In this study, this is described as a *vertical flat type* damage pattern for initial loading cycles. For a greater depth, the plastic deformation (damage) is reduced linearly to zero from 7 mm to around 11 mm to 12 mm sub-surface depth of railhead material. All endpost materials exhibit similar damage patterns in the sub-surface of the railhead after 50 loading cycles. However, for 1000 and 2000 loading cycles (Figures 7~8), the shallow sub-surface damage pattern is different to that of 50 loading cycles. A sharp change occurs in plastic deformation in the sub-surface depth. The *vertical flat damage* pattern changes to a *horizontal bell-shaped* pattern for this PE22 damage parameter. The peak value of the damage parameter is concentrated at 2 mm to 3 mm sub-surface depth, and the plots indicate that the fb is a better endpost material to control sub-surface railhead material damage, followed by ptfе and ny. At 2000 loading cycles, the railhead damage is higher compared to that of 1000 cycles in all endpost cases while keeping the same *horizontal bell-shaped* pattern. The cyclic effects on damage pattern are evident for a single endpost material (fb) for all three loading cycles (Figure 9). It shows how a ‘flat type damage pattern’ changes to the ‘bell-shaped pattern’ clearly. These damage patterns are newly identified by this study. The damage style to railhead material due to the influence of other endpost materials such as ny is worthy of determination. In the Figure 9, more damage occurs from 50 to 1000 loading cycles compared to that from 1000 to 2000 loading cycles. It suggests that a decay in ratchetting rate occurs [16, 24].

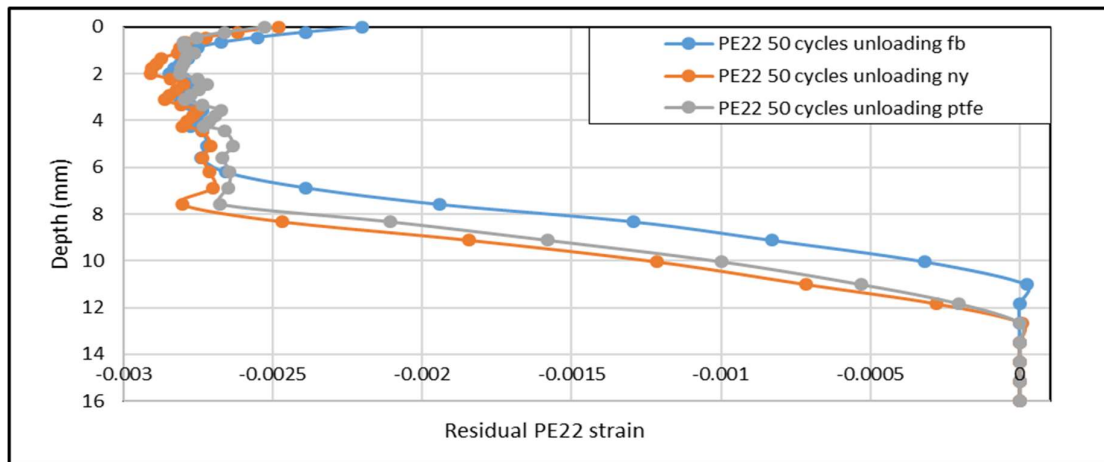


Figure 6: Residual PE 22 for fb, ny and ptfе at 50 loading cycles

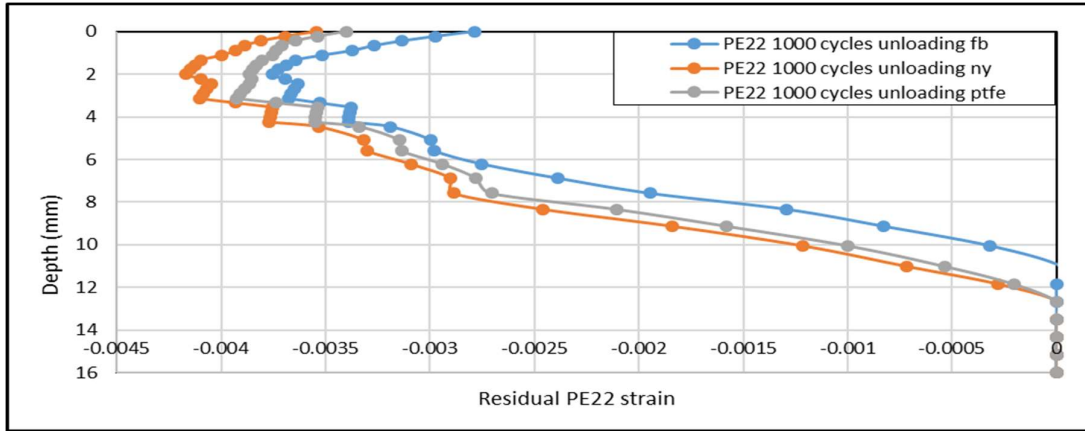


Figure 7: Residual PE 22 for fb, ny and ptfе at 1000 loading cycles

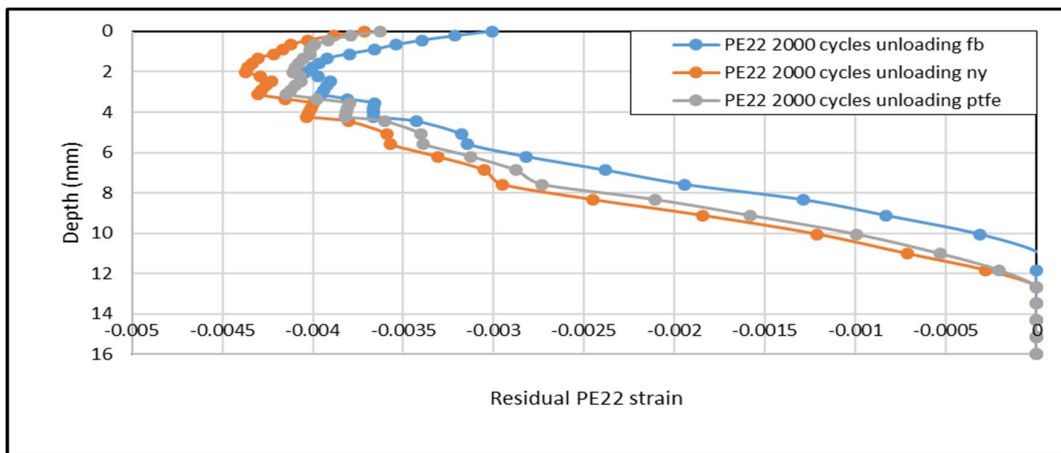


Figure 8: Residual PE 22 for fb, ny and ptfе at 2000 loading cycles

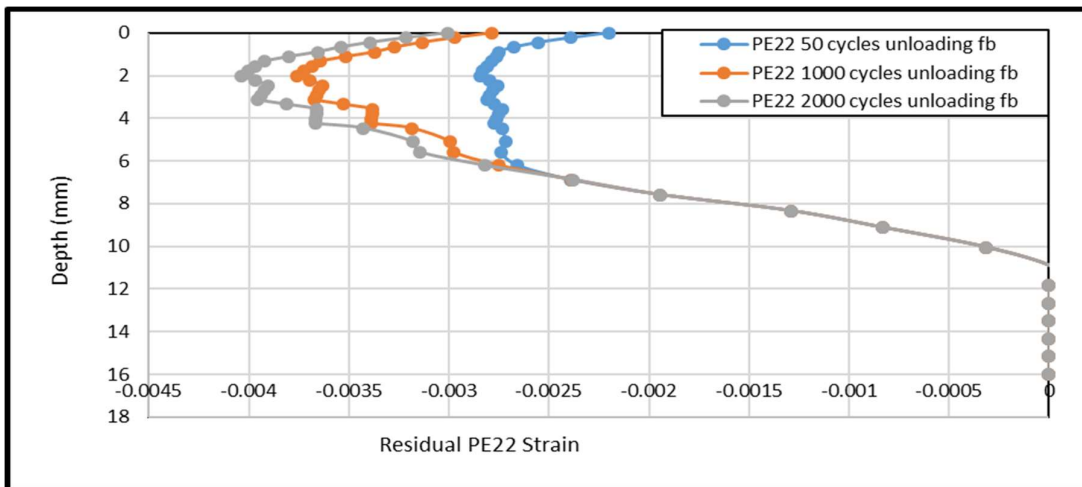


Figure 9: Residual PE22 for fb material at 50, 1000 and 2000 loading cycles

3.2 Stress results

Figures 10 to 12 present other damage parameters: the residual von-Mises stress component for the three endpost materials with Figure 10 for 50 loading cycles, Figure 11 for 1000 loading cycles and Figure 12 for 2000 loading cycles. For 50 loading cycles, the *vertical flat type* damage pattern exists from the top railhead surface to nearly 8 mm sub-surface depth of railhead for all three endpost materials. Then, the residual von-Mises component linearly reduces to zero at around 12 mm to 13 mm depth. At greater depth after this range, the material behaviour is fully elastic. Two important patterns, initially *vertical flat type* and then *inclined linear type* for the von-Mises damage parameter, are evident in Figure 10 as compared to the three patterns in Figure 6 of initial *inclined linear type*, then *vertical flat type* and finally *inclined linear type* again.

The *vertical flat pattern* of damage in Figure 10 at the shallow sub-surface depth changes as the number of loading cycles increase. For 1000 and 2000 loading cycles (Figures 11~12), a complex form of damage pattern exists: the new *horizontal bell-shaped pattern*. For both 1000 and 2000 loading cycles, less damage is seen for fb endpost material compared to that of ptfe and ny. As the number of cycles is increasing, more damage is occurring in the sub-surface rail material for all three endposts. This trend can be seen clearly in Figure 13 with an obvious change of damage pattern from 50 cycles to higher cycles for ptfe. A decay of damage rate is also evident, suggesting more damage occurs initially (from 50 cycles to 1000 cycles) and then reduces (from 1000 cycles to 2000 cycles). The decay of the ratchetting rate found in this study supports a trend found in previous studies [16, 24]. However, the change of the *vertically flat damage pattern* to a *horizontal bell-shaped pattern* is also evident for this damage parameter (residual von-Mises stress) for higher loading cycles as observed for PE22 (Figure 9). Considering these data, the endpost materials are ranked in the order of fb, ptfe and ny focusing on less sub-surface railhead material damage.

All data stated above suggest that fb endpost material, whose Young's Modulus is highest and Poisson's ratio is lowest among the three endpost materials considered, is better for controlling railhead sub-surface damage. The opposite is not true for the lowest performing endpost material (ny). Therefore, it is hard to propose a hypothesis directly relating sub-surface railhead material damage to elastic material properties (Young's Modulus and Poisson's ratio) considering these three endpost materials only. For a general statement, more endpost materials should be considered in the simulation. Other popular endpost materials are carbon fibre-epoxy resin, polycarbonate (pc), polystyrene (ps), polypropylene (pp), and aramid (kevlar 49).

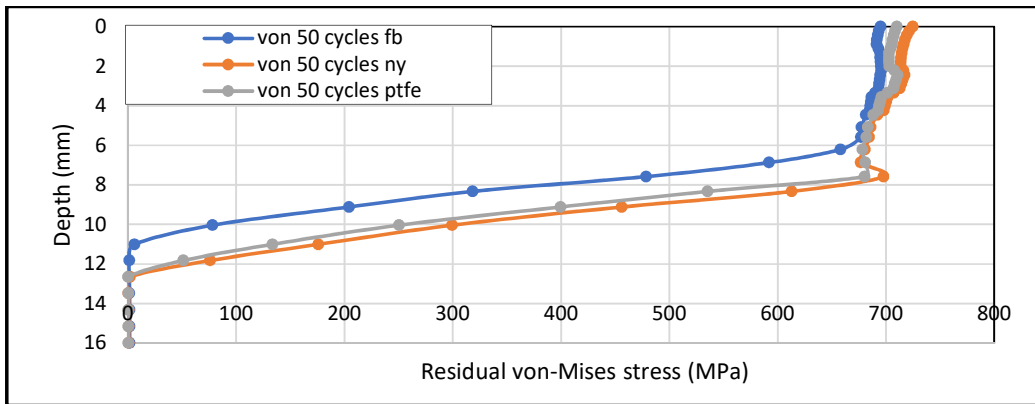


Figure 10: Residual von-Mises stresses for fb, ny and ptfe at 50 loading cycles

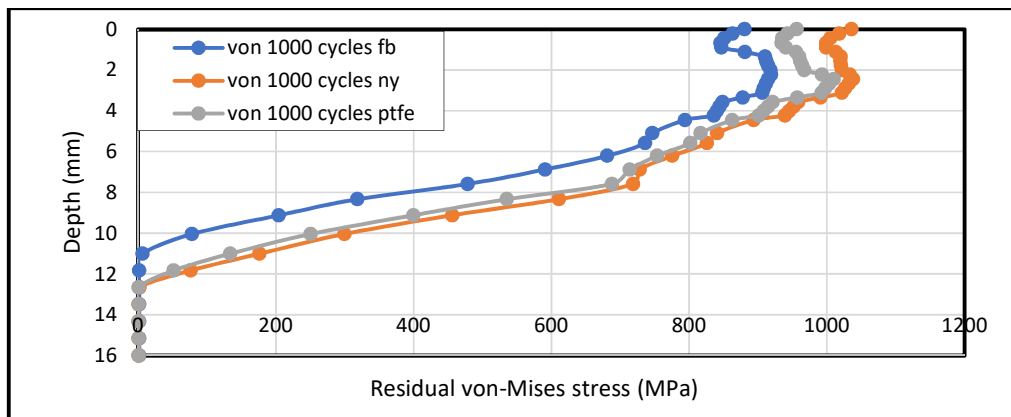


Figure 11: Residual von-Mises stresses for fb, ny and ptfe at 1000 loading cycles

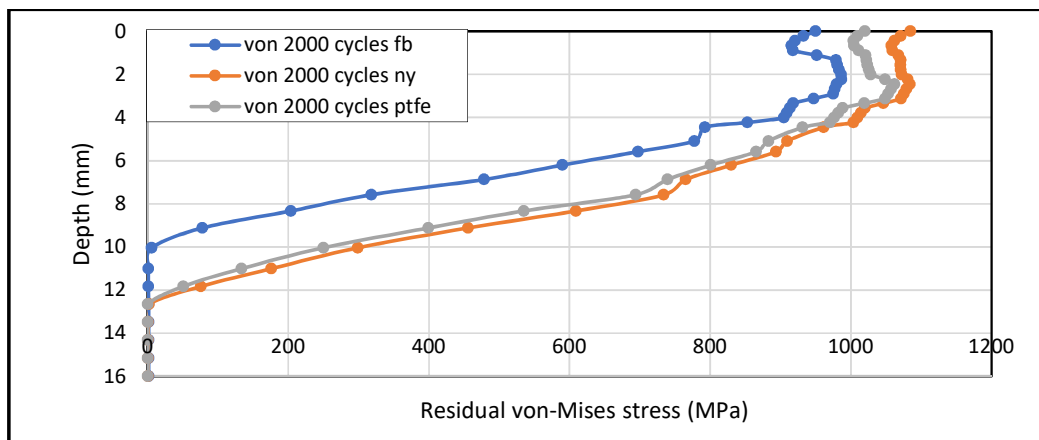


Figure 12: Residual von-Mises stresses for fb, ny and ptfe at 2000 loading cycles

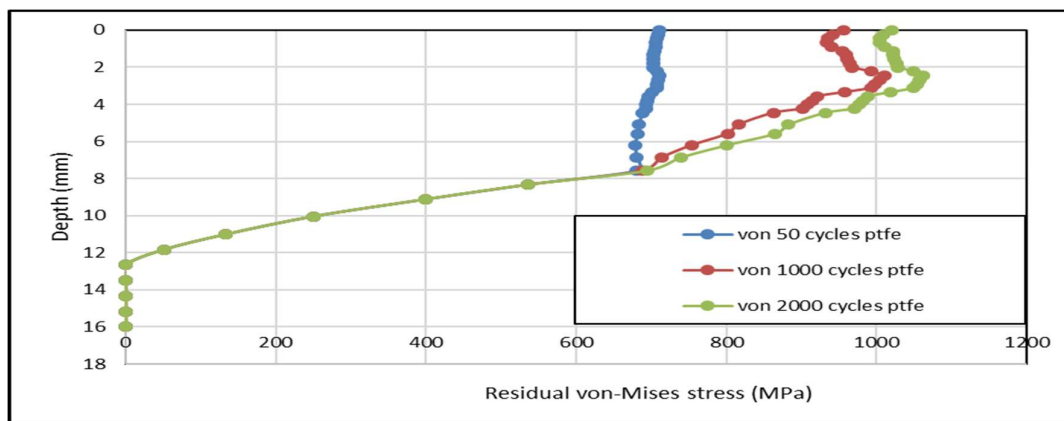


Figure 13: Residual von-Mises stresses for ptfе material at 50, 1000 and 2000 loading cycles

Explanations of the meaning of these new railhead material damage patterns observed in simulation results, namely the *vertical flat*, *horizontal bell-shaped*, and *inclined linear* patterns, are now put forward. Ringsberg [25] articulated that, for low traction wheel/rail contact, cracks were initiated in the shallow depth of railhead material because of high stress components. The variation of stresses and strains up to a depth of 16 mm below the top of the railhead, shown in Figures 6 to 13, indicate that railhead material damage occurs at relatively shallow depths up to about 13 mm and the plots maintain mixtures of *vertical flat*, *horizontal bell-shaped*, or *inclined linear* shaped patterns. For initial loading cycles once a new IRJ is installed in a railway track, the respective residual vertical strain and von-Mises stress components are nearly the same up to 6~7 mm sub-surface depth, with all simulation plots indicating the damage type as a *vertical flat type* pattern. As the number of loading cycles increase, the damage pattern changes to a curved style, which is called a *horizontal bell-shaped* pattern. Cracks can occur at very shallow depths of 2~3 mm below the top of the railhead [25]. For all numbers of loading cycles simulated, the residual strain PE22 and von-Mises stress components reduce linearly (*inclined linear* pattern) from approximately 8~10 mm up to 12~13 mm sub-surface depth of railhead material. Beyond this depth, the material behaviour is fully elastic and the damage that occurs is not because of ratchetting but due to elastic variation of stress and strain.

4.0 SIMULATION ACCURACY

4.1 Input output correlation

A contour plot of contact pressure on the IRJ is presented in Figure 14 (a) to show the simulation accuracy of the study. A vertical wheel load of 174kN was applied cyclically in a pressure form over the IRJ with a peak pressure of 2500MPa. The maximum pressure of 2412MPa for fb

endpost material is observed at the same location where a peak pressure of 2500MPa was used. The simulation error level is only 3.52% considering applied pressure and simulated pressure. The vertical stress S22 plot (Figure 14 (b)) presents a magnitude of 2432MPa at the same location where 2500MPa peak pressure load is applied vertically. The corresponding error level is 2.72%. Both results (Figure 14) suggest that the simulation data are deemed acceptable considering input-output correlation.

4.2 Laboratory testing

It is also necessary to validate any simulation results with results from laboratory tests incorporating the same input and support conditions, including loading (cyclic wheel loading of 174kN in pressure form) and other boundary conditions. Figure 15(a) shows the testing arrangement incorporating a loading patch representing a wheel of radius 425 mm on the IRJ with a fiberglass endpost of 5mm thickness. Figure 15(b) shows the location of the strain gauges used for comparison. The simulation results are compared with laboratory test results (Figure 16) employing a longitudinal strain gauge located on the top of the rail 100mm away from the endpost (Figure 15(b)). The test results of longitudinal strain (Figure 16) are for 20 cycles. A reasonable correlation is achieved with 14% error. This confirms that the methodology to generate the results presented previously has been validated.

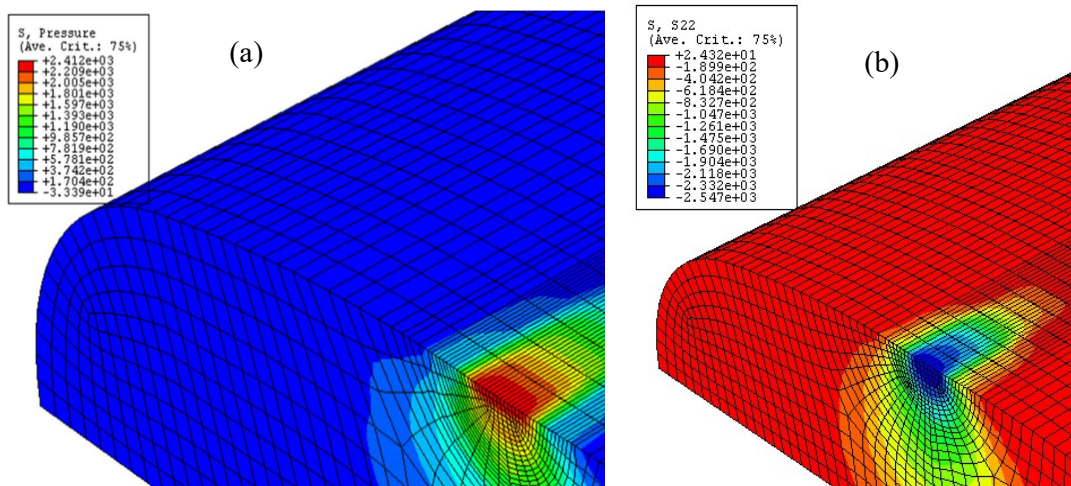


Figure 14: A contour plot of contact pressure on IRJ for fb endpost material at the end of 2000 loading cycles

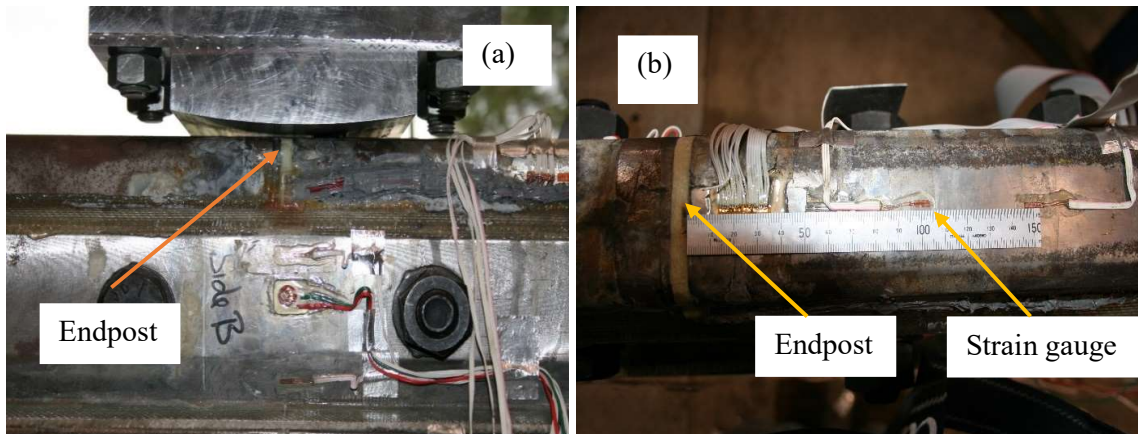


Figure 15: Laboratory testing: (a) loading on insulated rail joint, (b) location of strain gauge at the top surface of the rail (100mm away from endpost) used for verification

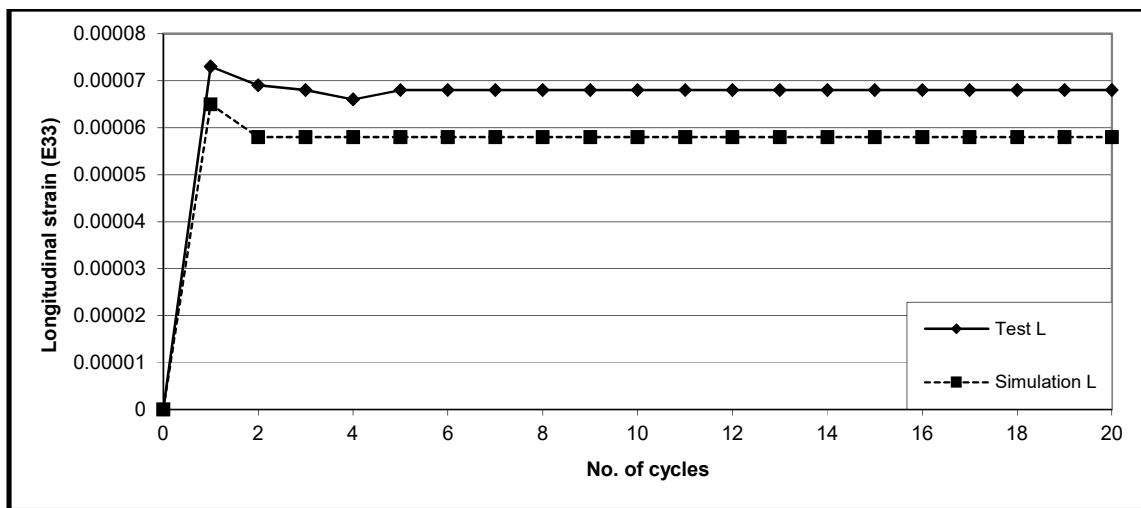


Figure 16: Longitudinal strain strains on rail top material at 100mm away from the endpost.

5.0 CONCLUSIONS

A detailed stress analysis was carried out on 6-bolt suspended IRJ design considering different endpost materials by applying a wheel loading that yields a contact stress over the yield strength of the rail steel. A wheel load of 174kN with a peak pressure load of 2500MPa was considered without any longitudinal creep force at the contact zone. A ratchetting material behaviour of the railhead material can be expected. The following conclusions can be made based on the observation of this study:

- At a shallow sub-surface depth, a ‘vertically flat type damage’ pattern is observed for all damage parameters due to 50 loading cycles.
- As the loading cycles increase, the ‘vertically flat damage pattern’ changes to a ‘horizontally bell-shaped damage’ pattern, for selected damage parameters.
- As the loading cycles increase, a decay in ratchetting rate is observed.
- Among the three endpost materials considered, fb is the best material relating to less sub-surface railhead material damage, followed by ptfе and ny.

ACKNOWLEDGEMENTS

Thanks go to Prof. M. Dhanasekar for his meticulous guidance to finish this research. Tim McSweeney, Adjunct Research Fellow, CRE is thankfully acknowledged for his advice at many stages of this ongoing study.

REFERENCES

- [1] S. Wise, D. Lindsay, I.G.T. Duncan, The strength of rails with particular reference to rail joints. *Proc. of Institution of Mechanical Engineers*, 174 (9) (1960) 371-407.
- [2] H.H. Jenkins, J.E. Stephenson, G.H. Clayton, G.W. Morland, D. Lyon, The effect of track and vehicle parameters on wheel/rail vertical dynamic force. *Railway Engineering Journal*, 3 (1974) 2-16.
- [3] Z. Yang, A. Boogaard, Z. Wei, J. Liu, R. Dollevoet, Z. Li, Numerical study of wheel-rail impact contact solutions at an insulated rail joint. *International Journal of Mechanical Sciences*, 138-139 (2018) 310-322.
- [4] M. Gallou, M. Forest, A. El-Hamalawi, C. Hardwick, Assessing the deflection behaviour of mechanical and insulated rail joints using finite element analysis. *Journal of Rail and Rapid Transit*, 232 (9) (2018) 2290-2308.
- [5] S.R. Lewis, R. Lewis, P.S. Goodwin, S. Fretwell-Smith, D.H. Fletcher, K. Murray, J. Jaiswal, Full-scale testing of laser clad railway track; Case study – testing for wear, bend fatigue and insulated block joint lipping integrity. *Wear*, 376-377 (2017) 1930-1937.
- [6] F.A. Elshukri, R. Lewis, An experimental investigation and improvement of insulated rail joints. *Tribology in Industry*, 38 (1) (2016) 121-126.
- [7] N.K. Mandal, FEA to assess plastic deformation of railhead material damage of insulated rail joints with fibreglass and nylon endposts. *Wear*, 366-367 (2016) 3-12.

- [8] N.K. Mandal, Finite element analysis of the mechanical behaviour of insulated rail joints due to impact loadings. *Journal of Rail and Rapid Transit*, 230(3) (2016) 759-773.
- [9] Y.Q. Sun, C. Cole, M. Spiryagin, Study on track dynamic forces due to rail short-wavelength dip defects using rail vehicle-track dynamics simulations. *Journal of Mechanical Sciences and Technology*, 27(3) (2013) 629-640.
- [10] Z. Wen, X. Jin, W. Zhang, Contact-impact stress analysis of rail joint region using the dynamic finite element method, *Wear*, 258(7-8) (2005) 1301-1309.
- [11] Z. Wen, G. Xiao, X. Xiao, X. Jin, M. Zhu, Dynamic vehicle-track interaction and plastic deformation of rail at rail welds, *Engineering Failure Analysis*, 16(4) (2009) 1221–1237.
- [12] P. Beaty, B. Temple, M.B. Marshall, R. Lewis, Experimental modelling of lipping in insulated rail joints and investigation of railhead material improvements, *Journal of Rail and Rapid Transit*, 230(4) (2016) 1375-1387.
- [13] N. Zong, M. Dhanasekar, Sleeper embedded insulated rail joints for minimising the number of modes of failure, *Engineering Failure Analysis*, 76 (2017) 27-43.
- [14] T.M. Bandula-Heva, M. Dhanasekar, P. Boyd, Experimental investigation of wheel/rail rolling contact at railhead edge, *Experimental Mechanics*, 53 (2013) 943-957.
- [15] T.M. Bandula-Heva, M. Dhanasekar, Failure of discontinuous railhead edges due to plastic strain, *Engineering Failure Analysis*, 44 (2014) 110-124.
- [16] N.K. Mandal, Ratchetting of railhead material of insulated rail joints (IRJs) with reference to endpost thickness. *Engineering Failure Analysis*, 45 (2014) 347-362.
- [17] N.K. Mandal, Influence of endpost materials on sub-surface railhead material damage of insulated rail joints due to wheel/rail contact loadings, *Proceeding of the Twenty-Second International Conference on Composite Materials (ICCM22)*, 11-16 August 2019, Melbourne, Australia.
- [18] N.K. Mandal, M. Dhanasekar, Sub-modelling for the ratchetting failure of insulated rail joints. *International Journal of Mechanical Science*, 75 (2013) 110-122.
- [19] J. Igwemezie, A.T. Nguyen, Anatomy of joint bar failures, *Railway Track and Structures*, July (2009) 31-37.
- [20] AS 1085.12: Railway track material: Insulated joint assemblies. (2002). Standards Australia.

- [21] N.K. Mandal, M. Dhanasekar, Y.Q. Sun, Impact forces at dipped rail joints. *Journal of Rail and Rapid Transit*, 230(1) (2016) 271-282.
- [22] N.K. Mandal, Ratchetting damage of railhead material of gapped rail joints with reference to free rail end effects. *Journal of Rail and Rapid Transit*, 231(2) (2017) 211-225.
- [23] N.K. Mandal, M. Spiriyagin, M. Berg, S. Stichel, On the railhead material damage of insulated rail joints: Is it by ratchetting or alternating plasticity? *International Journal of Fatigue*, 128, Nov. (2019) Paper no 105197.
- [24] N.K. Mandal, Plastic ratchetting of railhead material in the vicinity of insulated rail joints with wheel and thermal loads. *Wear*, 330-331 (2015) 540-553.
- [25] J.W. Ringsberg, Cyclic ratchetting and failure of a pearlitic rail steel. *Fatigue and Fracture of Engineering Materials and Structures*, 23 (2000) 747-758.